6th European Conference on Computational Mechanics (ECCM 6)
7th European Conference on Computational Fluid Dynamics (ECFD 7)
1115 June 2018, Glasgow, UK

A NUMERICAL TECHNIQUE FOR SOLVING THE OLDROYD-B MODEL FOR THE WHOLE RANGE OF VISCOSITY RATIOS

CAROLINE VIEZEL[1], MURILO F. TOMÉ[1], FERNANDO T. PINHO[2] AND SEAN MCKEE[3]

[1] Department of Applied Mathematics and Statistics, University of São Paulo
Av. Trabalhador São Carlense, 400, CEP 13560-270, São Carlos, Brazil
cviezel@usp.br, murilo@icmc.usp.br

[2] CEFT, Department of Mechanical Engineering, Faculty of Engineering , University of Porto
Rua Dr. Roberto Frias s/n, 4200-465, Porto, Portugal
fpinho@fe.up.pt

[3] Department of Mathematics and Statistics, University of Strathclyde
Glasgow, 26 Richmond Street, G11XH, U.K.
sean.mckee@strath.ac.uk

Key words: Oldroyd-B model, EVSS, Free surface, Finite difference, Drop impact

Abstract. This work presents a technique for simulating time-dependent axisymmetric free surface flows of Oldroyd-B fluids that is capable of solving the Oldroyd-B model for any value of the ratio $\beta = \lambda_2/\lambda_1$, in the interval $[0, 1]$. Thus, it can solve the purely elastic UCM model when $\beta = 0$ and reduces to Newtonian flow if $\beta = 1$. We employ the EVSS transformation $\boldsymbol{\tau} = \mathbf{S} + 2\eta_0\mathbf{D}$ where the extra-stress tensor $\boldsymbol{\tau}$ is the solution of the Oldroyd-B constitutive equation while the non-Newtonian tensor $\mathbf{S}$ is calculated as a function of $\boldsymbol{\tau}$ and $2\eta_0\mathbf{D}$. The Oldroyd-B tensor is related to the conformation tensor $\mathbf{A}$ which is approximated implicitly by a system of finite difference equations that is solved exactly. The methodology developed is a Marker-and-Cell type method that uses a staggered grid and solves the momentum equations using primitive variables and a discrete non-symmetric Poisson equation to obtain a divergence-free velocity field and the pressure within the fluid and on the free surface. To verify this new technique, tube flow is solved and the numerical predictions are compared with the analytical solution for fully developed flow; the convergence of the method is demonstrated via mesh refinement. The performance of this method is demonstrated by solving the impacting drop problem for which a study of the parameters involved is provided and new phenomena are reported.

1 INTRODUCTION

The importance of non-Newtonian free surface flows in industrial processes has attracted the attention of many scientists. Examples of such applications include polymer

processing in the plastic industry such as mold filling of complex cavities and filling of containers with viscoelastic fluids. These flows are represented by a system of nonlinear equations and the presence of moving free surfaces makes difficult to solve the corresponding governing equations and the associated boundary conditions using a computer code. An extra challenge comes from the fact that a unique constitutive equation can not model polymers in general. Indeed, a great number of differential constitutive equations that can accurately represent viscoelastic fluids have been developed over the past decades, as for example, Upper-Convected-Maxwell (UCM) [1], OLDROYD-B [2], Phan-Thien-Tanner (PTT) [3], Giesekus [4], various FENE type models [5], Extended Pom-Pom (Pom-Pom) [6, 7], among others. Apart from these differential models, integral constitutive equations have also been employed to simulate viscoelastic free surface flows [8, 9]. These are more advanced models that require sophisticated approaches to compute the solution of the integral-differential system of equations involved and for this reason, most numerical methods for solving viscoelastic flows employ differential constitutive equations. In particular, the differential form of the Upper-Convected-Maxwell (UCM) and the Oldroyd-B models have been extensively studied over the past decades. Numerical investigations of viscoelastic free surface flows modeled by these models using, for instance, finite element, finite volume and finite difference methods can be found in the following works [1, 10]–[23]

In this work, we present a new finite difference methodology to solve the governing equations for axisymmetric free surface flows governed by the Oldroyd-B model. The free surface of the fluid is dealt with a modified Marker-and-Cell method presented by Tomé et al. [16]. This new methodology is verified by solving fully developed tube flow together with mesh refinement studies. To demonstrate the capabilities of this new methodology in solving time-dependent free surface flows, the impacting drop problem of Oldroyd-B and UCM fluids is simulated.

2 GOVERNING EQUATIONS

The mass conservation and momentum equations are the basic equations for incompressible flows which can be written as,

$$\nabla \cdot \mathbf{v} = 0\,, \tag{1}$$

$$\rho\Big[\frac{\partial \mathbf{v}}{\partial t} + \nabla \cdot (\mathbf{v}\mathbf{v})\Big] = -\nabla p + \nabla \cdot \boldsymbol{\tau} + \rho \mathbf{g}\,, \tag{2}$$

where $\mathbf{v}$ is the velocity vector, p is the scalar pressure, $\mathbf{g}$ is the acceleration of gravity vector, ρ is the density of the fluid and $\boldsymbol{\tau}$ is the extra-stress tensor.

We are interested in flows governed by the Oldroyd-B rheological constitutive equation that can be expressed by the following equation

$$\boldsymbol{\tau} + \lambda_1 \overset{\triangledown}{\boldsymbol{\tau}} = 2\eta_0 \left[\mathbf{D} + \lambda_2 \overset{\triangledown}{\mathbf{D}}\right], \qquad \mathbf{D} = \frac{1}{2}\Big[(\nabla \mathbf{v}) + (\nabla \mathbf{v})^T\Big]\,, \tag{3}$$

where $\mathbf{D}$ is the rate-of-deformation tensor. The symbol $\overset{\triangledown}{\boldsymbol{\tau}}$ represents the upper-convected derivative given by

$$\overset{\triangledown}{\boldsymbol{\tau}} = \frac{\partial \boldsymbol{\tau}}{\partial t} + \nabla \cdot (\mathbf{v}\boldsymbol{\tau}) - \big(\nabla \mathbf{v}\big)\boldsymbol{\tau} - \boldsymbol{\tau}\big(\nabla \mathbf{v}\big)^T.$$

In Eq. (3), λ_1 is the relaxation time, $\lambda_2 = \lambda_1 \dfrac{\eta_S}{\eta_0}$ is the retardation time, $\eta_0 = \eta_P + \eta_S$ is the sum of solvent (η_S) and polymeric (η_P) viscosities. The ratio $\beta = \dfrac{\eta_S}{\eta_0}$ measures the quantity of solvent viscosity within the fluid. When $\beta = 0$, Eq. (3) reduces to the *Upper-Convected Maxwell* (UCM) model and if $\beta = 1$ we have *Newtonian* flow.

In this work, the extra-stress tensor $\boldsymbol{\tau}$ is related to the conformation tensor $\mathbf{A}$ by

$$\boldsymbol{\tau} = \frac{\eta_0}{\lambda_1}\big(1-\beta\big)\big(\mathbf{A}-\mathbf{I}\big) + 2\beta\eta_0\,\mathbf{D}\,, \tag{4}$$

where the conformation tensor $\mathbf{A}$ is evolved in time by solving

$$\mathbf{A} + \lambda_1 \overset{\nabla}{\mathbf{A}} = \mathbf{I}\,. \tag{5}$$

To solve the momentum equation (2), we employ the following transformation (known as EVSS [22])

$$\boldsymbol{\tau} = \mathbf{S} + 2\eta_0\mathbf{D}\,, \tag{6}$$

which after being introduced in the momentum equation (2) provides

$$\rho\Big[\frac{\partial \mathbf{v}}{\partial t} + \nabla\cdot(\mathbf{v}\mathbf{v})\Big] = -\nabla p + \eta_0\nabla^2\mathbf{v} + \nabla\cdot\mathbf{S} + \rho\mathbf{g}\,. \tag{7}$$

In this work, we propose a method that is able to obtain results for an value of $\beta \in [0\,,\,1]$. This method consists of calculating the extra-stress $\boldsymbol{\tau}$ using the conformation tensor $\mathbf{A}$ and then obtaining the non-Newtonian tensor $\mathbf{S}$ as a function of $\boldsymbol{\tau}$ and $\mathbf{D}$. Details of this technique are presented in the next Section.

2.1 Boundary conditions

The boundary conditions can be summarized as follows: on rigid boundaries the no-slip condition is imposed; on inflows, the velocity is prescribed while the extra-stress tensor obeys fully developed flow (details are given in Section 4). On outflows, homogeneous Neumann conditions are imposed for the velocity field. On the free surface, in the absence of surface tension, the boundary conditions are given by equations

$$\mathbf{n}^T\cdot(\boldsymbol{\sigma}\cdot\mathbf{n}) = 0\,, \qquad \mathbf{m}^T\cdot(\boldsymbol{\sigma}\cdot\mathbf{n}) = 0\,, \tag{8}$$

where, $\boldsymbol{\sigma} = -p\mathbf{I} + \mathbf{S} + 2\eta_0\mathbf{D}$ is the stress tensor and $\mathbf{n}$ and $\mathbf{m}$ are unity vectors normal and tangential to the free surface, respectively.

3 NUMERICAL METHOD

The equations presented in Section 2, which are specified in Section 3.1, are solved by the finite difference method on a staggered grid (Fig. 1a displays the locations of the variables in a cell). The fluid (also the free surface) is modeled by an improved Marker-and-Cell method developed by Tomé et al. [17] wherein the fluid surface is determined

by a closed linear spline that is defined by marker-particles (see Fig. 1b). To implement this technique it is necessary to divide the cells within the mesh to into several types as follows (see Fig. 1c):
▶ Rigid boundary (**B**): cells that define the location of rigid contours;
▶ Inflow boundary (**I**): cells that model 'fluid entrances' ('inflows');
▶ Outflow boundary (**O**): cells that define 'fluid exits' ('outflows');
▶ Empty cells (**E**): cells that do not contain fluid;
▶ Full cells (**F**): cells that contain fluid and have no contact with **E**-faces;
▶ Surface cells (**S**): cells that contain fluid and have at least one face in contact with **E**-faces.

3.1 Numerical algorithm

Equations (1), (7), (4), (5) and (6), written in cylindrical coordinates, are solved for the unknowns $u(r,z,t)$, $w(r,z,t)$, $p(r,z,t)$, $\mathbf{S}(r,z,t)$, $\boldsymbol{\tau}(r,z,t)$ and $\mathbf{A}(r,z,t)$, as follows. These equations are used in dimensionless form and contain the nondimensional numbers $Re = \dfrac{\rho_0 U L}{\eta_0}$ (*Reynolds* number), $Wi = \lambda_1 \dfrac{U}{L}$ (*Weissenberg* number) and $Fr = \dfrac{U}{\sqrt{L\,g}}$ (*Froude* number), in which L and U are typical scales for velocity and length, respectively, ρ_0 is the fluid density and g is the acceleration of gravity (for details see [16]).

The computational cycle is performed in three steps, as follows:
STEP1: Calculation of $\mathbf{v}^{n+1} = \mathbf{v}(r,z,t_{n+1})$ and $p^{n+1} = p(r,z,t_{n+1})$

The algorithm for calculating $\mathbf{v}^{n+1}$ and p^{n+1} employs some ideas of the technique presented by Tomé et al. [16] that is briefly described next.

The pressure field is uncoupled from the mass (1) and momentum (7) equations by using the projection method of Chorin [24].
Let δt be the time step used, $t_{n+1} = t_n + \delta t$, and $\mathbf{v}^n = \mathbf{v}(r,z,t_n)$, $\boldsymbol{\tau}^n = \boldsymbol{\tau}(r,z,t_n)$ be known at time t_n. First, define $\mathbf{D}^n = \dfrac{1}{2}\Big[(\nabla \mathbf{v}^n) + (\nabla \mathbf{v}^n)^T\Big]$, $\mathbf{A}^n = \mathbf{I} + \dfrac{Re\,Wi}{1-\beta}\boldsymbol{\tau}^n - 2Wi\dfrac{\beta}{1-\beta}\mathbf{D}^n$ and $\mathbf{S}^n = \boldsymbol{\tau}^n - \dfrac{2}{Re}\mathbf{D}^n$. A tentative velocity field $\widetilde{\mathbf{v}}^{n+1}$ is then calculated by the implicit Euler method applied to the momentum equation by solving

$$\frac{\widetilde{\mathbf{v}}^{n+1} - \mathbf{v}^n}{\delta t} + \nabla \cdot (\mathbf{v}\mathbf{v})^n = -\nabla p^n + \frac{1}{Re}\nabla^2 \widetilde{\mathbf{v}}^{n+1} + \nabla \cdot \mathbf{S}^n + \frac{1}{Fr^2}\mathbf{g}\,. \tag{9}$$

It can be shown [25] that this velocity field contains the correct vorticity at time t but it does not conserve mass in general. Thus, a potential function $\psi(r,z,t_{n+1})$ is computed such that

$$\nabla^2 \psi^{n+1} = \nabla \cdot \widetilde{\mathbf{v}}^{n+1}\,. \tag{10}$$

The final velocity field $\mathbf{v}^{n+1}$ is calculated from,

$$\mathbf{v}^{n+1} = \widetilde{\mathbf{v}}^{n+1} - \nabla \psi^{n+1}\,. \tag{11}$$

Therefore, $\mathbf{v}^{n+1}$ conserves mass and the vorticity remains unchanged.

In this work, we use some concepts of the implicit technique of Oishi et al. [13] that couples the boundary condition for the pressure on the free surface given by Eq. (8) and the mass conservation equation Eq. (1). This technique consists of applying the mass conservation equation together with the pressure condition on the free surface and the equation for the velocity $\mathbf{v}^{n+1}$ on surface cells. By doing this, new equations for the potential function ψ^{n+1} are derived and added to the set of equations originated by the discrete version of the Poisson equation Eq. (10), resulting in an asymmetric linear system that is solved by the Bi-conjugate gradient method. After obtaining ψ^{n+1}, the pressure is calculated by

$$p^{n+1} = p^n + \frac{\psi}{\delta t}. \tag{12}$$

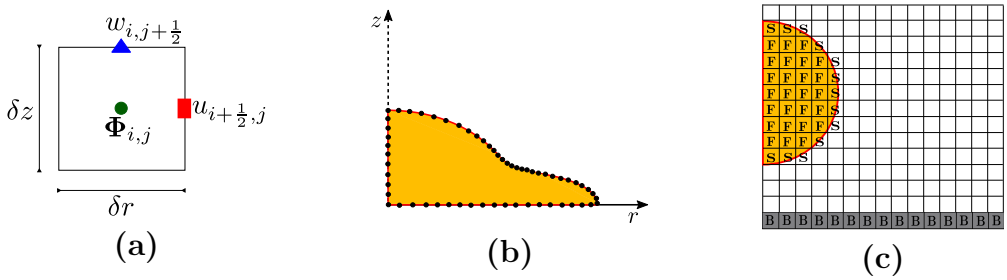

Figure 1: (a) Description of the cell employed in the mesh, (b) Representation of fluid free surface (line connecting the particles) and volume of fluid (yellow area), (c) Type of cells in the domain.

STEP2: Calculation of $\boldsymbol{\tau}^{n+1} = \boldsymbol{\tau}(r, z, t_{n+1})$, $\mathbf{A}^{n+1} = \mathbf{A}(r, z, t_{n+1})$ and $\mathbf{S}^{n+1} = \mathbf{S}(r, z, t_{n+1})$

In this step we first calculate the conformation tensor $\mathbf{A}^{n+1} = \mathbf{A}(r, z, t_{n+1})$ by solving Eq. (5) using finite differences. Equation (5) is solved implicitly by the equation

$$\frac{\mathbf{A}^{n+1} - \mathbf{A}^n}{\delta t} - (\nabla \mathbf{v}^{n+1})^T \mathbf{A}^{n+1} - \mathbf{A}^{n+1}(\mathbf{v}^{n+1}) + \frac{1}{Wi}\mathbf{A}^{n+1} = -\nabla \cdot (\mathbf{v}^{n+1}\mathbf{A}^n) + \frac{1}{Wi}\mathbf{I}. \tag{13}$$

By writing this equation in component form, the following 4×4 linear system

$$\begin{bmatrix} a_{11} & 0 & 0 & a_{14} \\ 0 & a_{22} & 0 & 0 \\ 0 & 0 & a_{33} & a_{34} \\ a_{41} & 0 & a_{43} & a_{44} \end{bmatrix} \begin{bmatrix} A^{rr} \\ A^{\theta\theta} \\ A^{zz} \\ A^{rz} \end{bmatrix}^{n+1} = \begin{bmatrix} F_1 \\ F_2 \\ F_3 \\ F_4 \end{bmatrix}, \tag{14}$$

is obtained and has to be solved for each cell in the mesh. The matrix coefficients and the right hand side of this linear system are given by

$$
\begin{aligned}
a_{11} &= 1.0 + \frac{\delta t}{Wi} - 2\delta t \frac{\partial u^{n+1}}{\partial r}, & a_{14} &= -2\delta t \frac{\partial u^{n+1}}{\partial z}, \\
a_{22} &= 1.0 + \frac{\delta t}{Wi} - 2\delta t \frac{u^{n+1}}{r}, & a_{33} &= 1.0 + \frac{\delta t}{Wi} - 2\delta t \frac{\partial w^{n+1}}{\partial z}, \\
a_{34} &= -2\delta t \frac{\partial w^{n+1}}{\partial r}, & a_{41} &= -\delta t \frac{\partial w^{n+1}}{\partial r}, \\
a_{44} &= 1.0 + \frac{\delta t}{Wi} - 2\delta t \Big(\frac{\partial w^{n+1}}{\partial z} + \frac{\partial u^{n+1}}{\partial r} \Big), & a_{43} &= -\delta t \frac{\partial u^{n+1}}{\partial z},
\end{aligned}
\tag{15}
$$

$$
\begin{aligned}
F_1 &= (A^{rr})^n + \delta t \left[\frac{1}{Wi} - \frac{1}{r} \frac{\partial (r u^{n+1} (A^{rr})^n)}{\partial r} + \frac{\partial (w^{n+1} (A^{rr})^n)}{\partial z} \right], \\
F_2 &= (A^{\theta\theta})^n + \delta t \left[\frac{1}{Wi} - \frac{1}{r} \frac{\partial (r u^{n+1} (A^{\theta\theta})^n)}{\partial r} + \frac{\partial (w^{n+1} (A^{\theta\theta})^n)}{\partial z} \right], \\
F_3 &= (A^{zz})^n + \delta t \left[\frac{1}{Wi} - \frac{1}{r} \frac{\partial (r u^{n+1} (A^{zz})^n)}{\partial r} + \frac{\partial (w^{n+1} (A^{zz})^n)}{\partial z} \right], \\
F_4 &= (A^{rz})^n + \delta t \left[\frac{1}{Wi} - \frac{1}{r} \frac{\partial (r u^{n+1} (A^{rz})^n)}{\partial r} + \frac{\partial (w^{n+1} (A^{rz})^n)}{\partial z} \right].
\end{aligned}
\tag{16}
$$

The derivatives in Eq. (15) are approximated by second order finite differences while the convective terms in Eq. (16) are calculated by the high order stable upwind method CUBISTA [15]. The use of this high order bounded upwind method and small time-steps provide accurate solution for the conformation tensor $\mathbf{A}$. The solution of the system (14) is obtained analytically by

$$
\begin{aligned}
[A^{\theta\theta}]^{n+1} &= \frac{F_2}{a_{22}}, \qquad [A^{rz}]^{n+1} = \frac{F_4 - \frac{a_{41}}{a_{11}} F_1 - \frac{a_{43}}{a_{33}} F_3}{a_{44} - \frac{a_{41}}{a_{11}} a_{14} - \frac{a_{43}}{a_{33}} a_{34}}, \\
[A^{rr}]^{n+1} &= \frac{1}{a_{11}} \Big[F_1 - a_{14} [A^{rz}]^{n+1} \Big], \qquad [A^{zz}]^{n+1} = \frac{1}{a_{33}} \Big[F_3 - a_{34} [A^{rz}]^{n+1} \Big].
\end{aligned}
\tag{17}
$$

Therefore, the tensor $\boldsymbol{\tau}^{n+1}$ is given by

$$
\boldsymbol{\tau}^{n+1} = \frac{1}{Re\, Wi} \big(1 - \beta\big) \big(\mathbf{A}^{n+1} - \mathbf{I} \big) + \frac{2}{Re} \beta\, \mathbf{D}^{n+1}\,, \tag{18}
$$

and the non-Newtonian tensor $\mathbf{S}^{n+1}$ is computed from

$$
\mathbf{S}^{n+1} = \boldsymbol{\tau}^{n+1} - \frac{2}{Re} \mathbf{D}^{n+1}\,. \tag{19}
$$

STEP3: The last step in the calculational cycle is to move the marker-particles to their new positions by solving

$$
\frac{dr}{dt}\Big|_{\mathbf{P}} = u(r,z)^{n+1}_{\mathbf{P}}; \qquad \frac{dz}{dt}\Big|_{\mathbf{P}} = w(r,z)^{n+1}_{\mathbf{P}}, \tag{20}
$$

for each particle $\mathbf{P} = [r_{\mathbf{P}}\ z_{\mathbf{P}}]^T$. The particle velocity $\mathbf{V_P} = [u(r,z)^{n+1}_{\mathbf{P}}\ v(r,z)^{n+1}_{\mathbf{P}}]^T$ is found by a bilinear interpolation using the nearest velocities. For details see Tomé et al. [16].

4 VERIFICATION RESULTS

To verify the numerical method described in Section 3, fully developed *Poiseuille* flow in a tube was simulated and the numerical predictions were compared with the analytic solutions.

A tube of radius $R = 1.0\,\mathrm{m}$ and length $H = 10R\,\mathrm{m}$ composed the computational domain $\Omega = [0\,,\,R] \times [0\,,\,10R]$ as illustrated in Fig. 2b. The tube was empty and fluid was injected at the inflow with the imposition of the following fully developed profile:

$$\begin{aligned} w(r) = \big(1 - r^2\big), \qquad u(r) = 0, \qquad \dot{\gamma} = \frac{dw}{dr} = -2r, \\ \tau^{zz}(r) = \frac{2}{Re} Wi \big(1-\beta\big)\dot{\gamma}^2, \qquad \tau^{rz}(r) = \frac{1}{Re}\dot{\gamma}, \qquad \tau^{rr}(r) = \tau^{\theta\theta}(r) = 0. \end{aligned} \tag{21}$$

The input data were: $L = R = 1\mathrm{m}$, $U = 1\mathrm{ms}^{-1}$, $\rho = 1000\mathrm{kg\,m}^{-3}$, $\eta_0 = 4.0\mathrm{Pa.s}$, $\lambda_1 = 1.0\mathrm{s}$ and $\lambda_2 = 0.2\mathrm{s}$ ($\beta = 0.2$). Therefore, $Re = \dfrac{\rho\, U\, L}{\eta_0} = 0.25$ and $Wi = \lambda_1 \dfrac{U}{L} = 1.0$. By using the meshes presented on Table 1, this problem was simulated until time $t(U/L) = 100.0$ on each mesh.

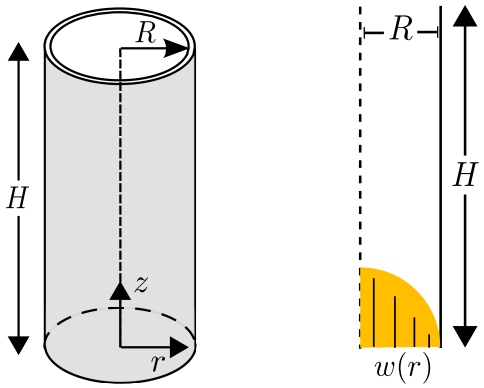

Figure 2: Description of flow domain (a) and computational domain (b).

Table 1: Meshes used to simulate tube flow.

Mesh	M10	M20	M30
$\delta_r = \delta_z$	0.1000	0.0500	0.0333
Cells in the mesh	(10×100)	(20×200)	(30×300)

Fig. 3 displays the numerical solutions obtained for $w(r, z_m)$, $\tau^{zz}(r, z_m)$ and $\tau^{rz}(r, z_m)$. These solutions are plotted at the middle of the tube at $z_m = 0.5H$. For comparisons, the analytic solutions are also plotted in Fig. 3. It can be seen that the numerical solutions agree well with the corresponding solutions on the meshes employed. Moreover, Table 2 shows that the errors calculated with the norm defined by Eq. (22) decay with mesh

refinement and the calculated convergence orders are about two. This is in accordance with the second-order finite difference approximations employed to solve the equations.

$$E(\cdot) = \sqrt{h \sum \left[(\cdot)_{analytic} - (\cdot)_{numerical}\right]^2}, \quad h = \delta_r = \delta_z, \tag{22}$$

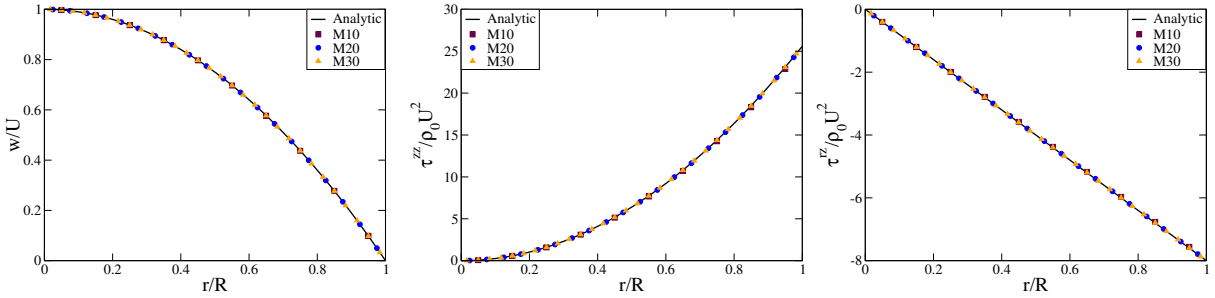

(a) (b) (c)

Figure 3: Comparison of (a) $w(r)$; (b) $\tau^{zz}(r)$ and (c) $\tau^{rz}(r)$ obtained on meshes M10, M20 and M30 with the respective analytic solution of *Poiseuille* flow.

Table 2: Errors between analytic and numerical solutions calculated on meshes M10, M20, M30.

Errors				Orders	
Mesh	M10	M20	M30	O(M10,M20)	O(M20,M30)
$w(r, z_m)$	1.683826e-03	4.260340e-04	1.898501e-04	1.982703	1.993475
$\tau^{rz}(r, z_m)$	2.280432e-02	5.749979e-03	2.559584e-03	1.987679	1.99611
$\tau^{zz}(r, z_m)$	1.124021e-01	2.845901e-02	1.267881e-02	1.981711	1.994088

5 Simulation of drop impacting

We simulated the time-dependent deformation of a spherical drop containing an Oldroyd-B fluid after it impacted a rigid disk. This problem was chosen to establish our method on complicated time-dependent free surface flows. Moreover, it is usually employed to test the efficiency of numerical algorithms on problems having large free surface deformations and a comparison with solutions obtained by other techniques can be effected.

We considered a drop of diameter $d = 2R$ that is positioned above a circular disk at a height H (see Fig. 4b). At $t = 0$ the drop starts flowing downwards with initial velocity $w(r, z, 0) = -U$. After the drop impacts the disk it starts to flow radially expanding its diameter $d(t)$ while, after a short period of time, due to elasticity forces, it is expected that it will contract, decreasing its diameter $d(t)$. We are interest to study the effects of the parameters Wi and β on the variation of the drop diameter $d(t)$ with time.

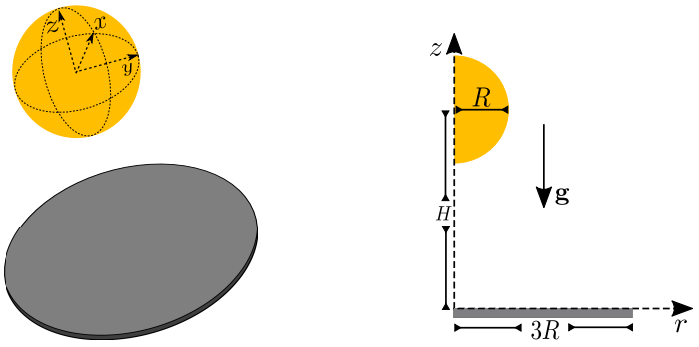

(a) (b)

Figure 4: Simulation of drop impacting. (a) 3D view of initial state; (b) Computational domain employed.

Table 3: Input data (SI units) used in the impacting drop simulation.

$d = 2R$ $[m]$	H $[m]$	U $[m^{-1}]$	λ $[s]$	η_0 $[Pa.s]$	ρ $[kg\,m^{-3}]$	g $[m\,s^{-2}]$	Fr
0.02	0.04	1.0	0.02	4.0	1000.0	-9.81	2.2576

Table 4: Meshes employed in the simulation of drop impacting.

Mesh	M10	M16	M20	M30	M40
spacing (h/d)	0.050000	0.031250	0.025000	0.016666	0.012500

5.1 Verification results

To verify our code, we performed a mesh refinement followed by comparisons with results from other investigators. The data used in these simulations were $Re = 5$, $Wi = 1.0$, $\beta = 0.1$ together with the data from Table 3 and carried out simulations until time $t*(U/d) = 5.0$ employing the meshes defined in Table 4. The results obtained are displayed in Fig. 5a where it can be seen that the solutions on the coarser meshes converge to those on the finest mesh (M40). Moreover, Fig. 5b presents a comparison of $d(t)$ with the results obtained by Figueiredo et al. [19], Xu et al. [20] and OpenFOAM [21]. It can be observed that the time evolution of $d(t)$ obtained by our code agrees well with the results of Figueiredo et al., Xu et al. and the OpenFOAM code. These results verifies the proposed new method on this particular unsteady free surface flow.

5.2 Simulation of drop impacting

To demonstrate the capabilities of this new technique in simulating time-dependent viscoeslastic free surface flows, the input data displayed in Table 3 and mesh M40 were employed to simulate the impacting drop problem varying the parameters: β and Wi. Firstly, we used $Re = 5$ and $Wi = 1$ and simulated the drop impacting for the following values of β : $0, 0.001, 0.01, 0.02, 0.1, 0.3, 0.5, 0.7, 0.9$. The Newtonian flow corresponding to $\beta = 1$ was also simulated for reference. These simulations were performed until the nondimensional time $t * (U/d) = 20$.

Figure 6a displays the time history of $d(t)$ for each value of β. We can observe that the results with $\beta = 0.9$ are similar to the Newtonian drop and show that after the drop impacted the disk, at time $t \approx 1.4$, it continued to flow radially over the time, monotonically increasing $d(t)$. The results with $\beta = 0.7, 0.5, 0.3$ display a small expansion/contraction of the drop that occurred at times $t \approx 1.4$ and $t \approx 2.4$, respectively. It is seen that, after the contraction, the drop flowed radially, monotonically increasing $d(t)$, similar to the Newtonian drop. For $\beta = 0.1, 0.02, 0.01, 0.001$, the behaviour of $d(t)$ is more impressive. The higher elasticity within the drop makes it to expand/contract twice. These expansions/contractions become stronger as the value of β is reduced and for $\beta = 0.001$, the diameter $d(t)$ is about the same as that obtained with the UCM model ($\beta = 0$). This is in agreement with the Oldroyd-B model as it reduces to the UCM model when $\beta = 0$.

To observe the effect of a high Weissenberg number on the spreading of the drop, several simulations using $Re = 5.0$, $Wi = 20$ and $\beta = 0.01, 0.1, 0.3, 0.5, 0.7, 0.9$ were performed. The evolutions of $d(t)$ obtained in these simulations are displayed in Fig. 6b for each value of β. It is seen that, after the drop impacted the disk, the values of $d(t)$ corresponding to $\beta = 0.9, 0.7, 0.5, 0.3$ increase monotonically in time and do not present any contraction. However, for $\beta = 0.1, 0.01$ the diameter $d(t)$ presents large expansions, namely, $d(t) > 2.5d$ for $\beta = 0.01$ and $d(t) > 2d$ at $\beta = 0.1$. An interesting point is that for these values of β the diameter of the drop contracted to the same value of $d(t) \approx 0.04 = 2d$.

To show that the surface of the drop undergoes large deformations during the free surface flow, Fig. 7 displays a three-dimensional view of the unsteady flow of the drop over the disk for $Re = 5$, $\beta = 0.01$ and $Wi = 1, 20$. We can observe that the drop, with $Wi = 1$ (see the left column with 3D visualisations), initially expands until time $t = 2.6$ and from this time it retains contracting up to the time of $t = 3.4$ when an elevation at the centre of the drop can be seen (see the associated 3D view). After this time, the drop again starts to expand, making its centre to undergo a depression at $t \approx 3.8$ (see the associated 3D view) and at a later time $t = 4.6$, due to a contraction, a small elevation occurs at the centre of the drop. After this time the velocities within the drop became small and the drop surface did not present any change. We believe that the effects of expansion/contraction are due to elastic forces acting within the drop.

The results obtained with $Wi = 20$ are more dramatic. The high elasticity of the fluid provides more momentum to the drop so that its spreading is much more accentuated. It is seen that after the maximum spread, at time $t = 3.1$, there is a thin layer of fluid over the disk that is affected by elastic forces making the drop to contract until time $t = 5.3$ when a small jet emerges from the drop. Afterwards, the drop starts to expand again spreading over the disk.

6 CONCLUSIONS

This work presented a novel numerical algorithm to solve the Oldroyd-B model for free surface flows. The main feature of the formulation employed to solve the governing equations is the application of a splitting transformation that avoided the appearance of the viscosity ratio β in the momentum equations. The solution of the Oldroyd-B constitutive equation was obtained in terms of the conformation tensor $\mathbf{A}$ that was solved

implicitly. The method was verified against fully developed tube flow of Oldroyd-B fluids and convergence results were provided. The efficiency of this new methodology on unsteady free surface flow was attested by simulating the impacting drop problem for which mesh refinement and comparison with results from the literature were performed. The proposed method can easily be extended to three-dimensional flows and be used to solve any viscoelastic flow where the usual rheological splitting of the extra-stress tensor is employed.

7 ACKNOWLEDGEMENTS

The authors would like to acknowledge the financial support given by the funding agencies: CNPq - Conselho Nacional de Desenvolvimento Científico e Tecnológico Grant No. 306280/2014-0 and 150282/2017-6, FAPESP Grant No. 2013/07375-0 (CEPID-CeMEAI project) and CAPES Grant No. PROEX-9259544/D.

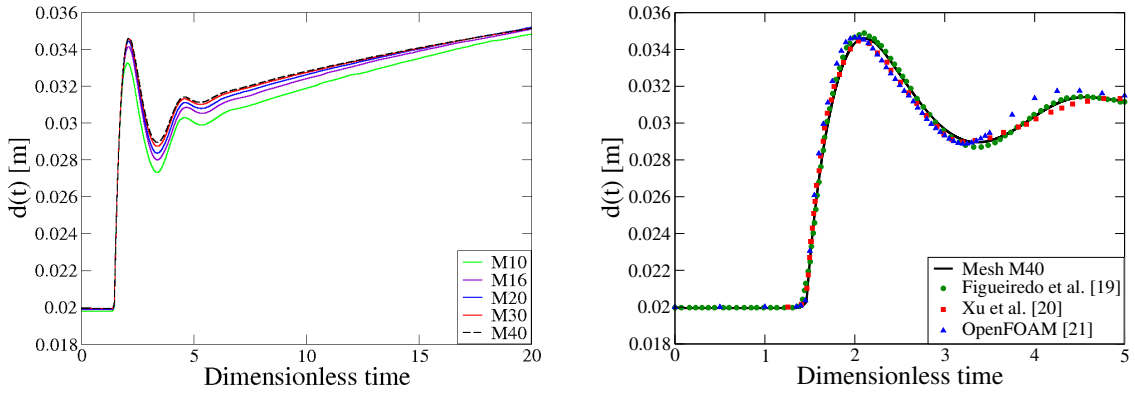

(a) (b)

Figure 5: Simulation of a drop impacting a disk - $Re = 5$, $Wi = 1$, $\beta = 0.1$. (a) Mesh refinement; (b) Comparison with other investigators. Our results were obtained on mesh M40.

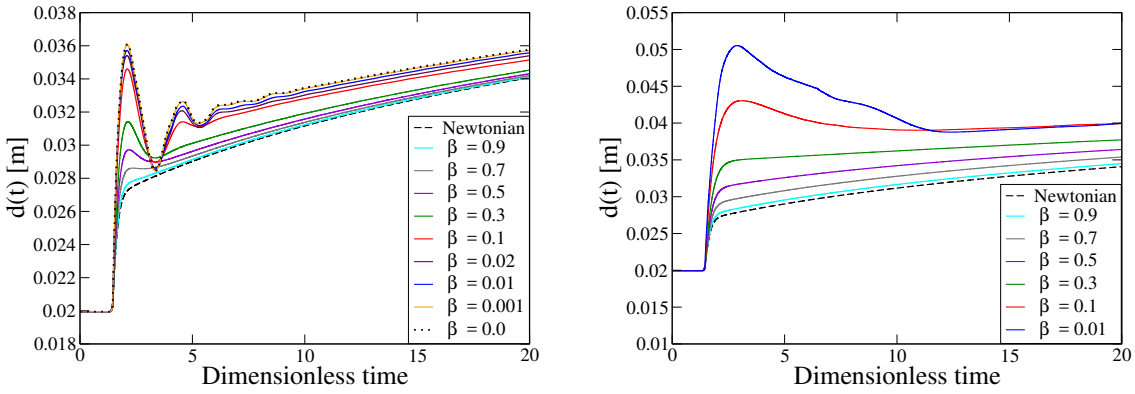

(a) (b)

Figure 6: Simulation of drop impacting a disk with $Re = 5$ and variation of β: (a) $Wi = 1$, (b) $Wi = 20$.

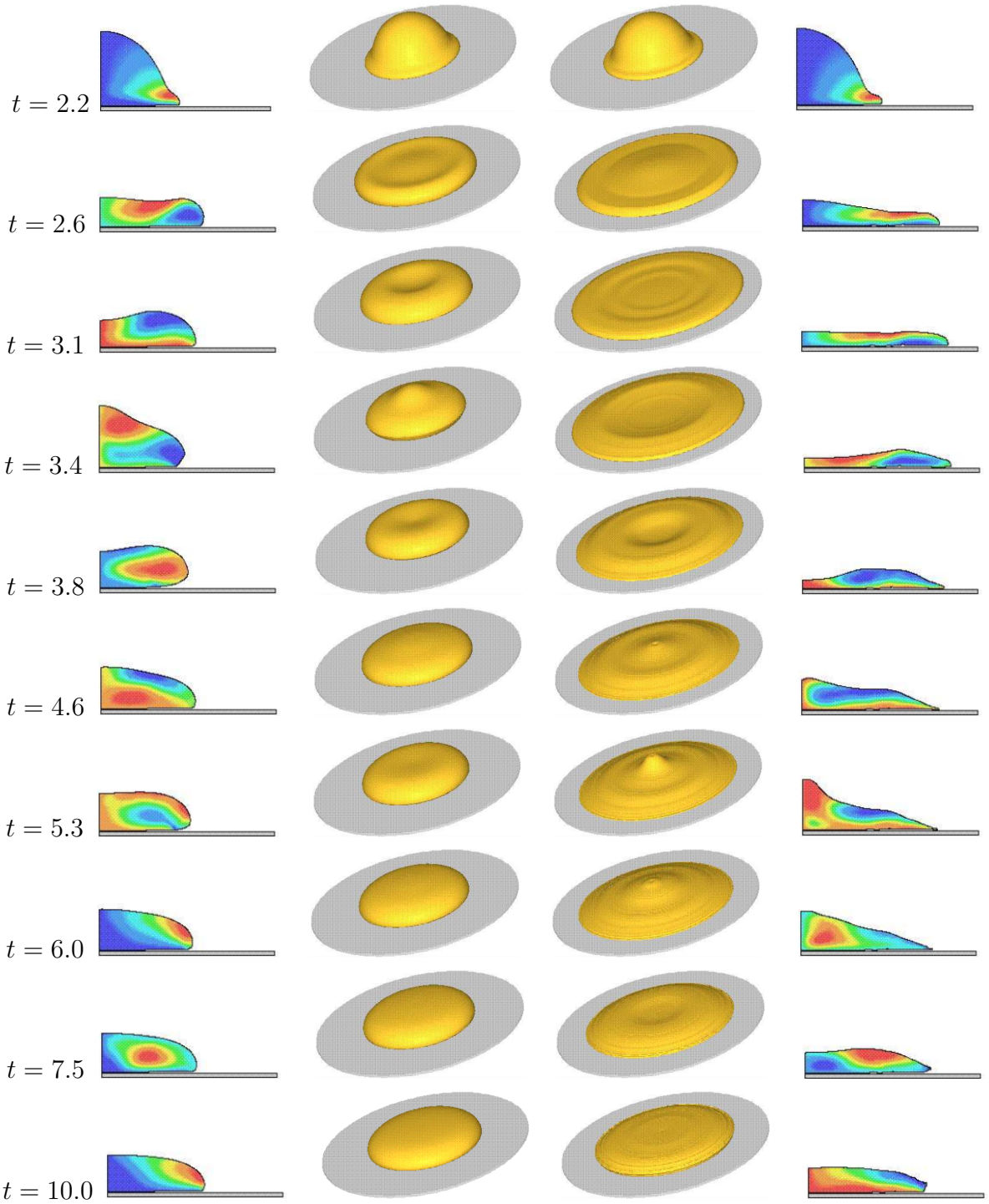

Figure 7: Simulation of a drop spreading over a disk - $Re = 5$, $\beta = 0.01$ and $Wi = 1, 20$, at selected times (from top to bottom) $t * (U/d) = 2.2, 2.6, 3.1, 3.8, 4.6, 5.3, 6.0, 7.5, 10.0$. 2D plots on the right and left sides display the u-velocity where the blue colour refers to negative values and the red colour stands for positive values.

REFERENCES

[1] R. G. Owens, T. N. Phillips, (2002). Computational Rheology. Imperial College Press. ISBN 978-1-86094-186-3.

[2] Oldroyd, James Clerk , On the Formulation of Rheological Equations of Estate, Proceedings of the Royal Society of London, Series A, Mathematical and Physical Sciences, **200** (1950) (1063): 523-541.

[3] R. I. Tanner, A theory of die-swell, Journal of Polymer Science, **8** (1970), 2067-2078.

[4] H. Giesekus, A simple constitutive equation for polymer fluids based on the concept of deformation-dependent tensorial mobility, Journal of Non-Newtonian Fluid Mechanics, **11** (1982), 69-109.

[5] R. B. Bird , R. C. Armstrong, O. Hassager, Dynamics of Polymeric Liquids, vol. 2, Wiley, New York, 1987.

[6] T. C. B. McLeish, R. G. Larson, Molecular constitutive equations for a class of branched polymers: The pom-pom polymer, Journal of Rheology, **42** (1998), 81-

[7] W. M. H. Verbeeten, G. W. M. Peters, F. P. T. Baaijens, Differential constitutive equations for polymer melts: the extended Pom-Pom model, Journal of Rheology, **45** (2001), 823-843.

[8] A. C. Papanastasiou, L. E. Scriven, C. W. Macosko, An integral constitutive equation for mixed flows: viscoelastic characterization, Journal of Rheology, **27** (1983), 387-410.

[9] X. L. Luo, E. Mitsoulis, An efficient algorithm for strain history tracking in finite element computations of non-Newtonian fluids with integral constitutive equations, International Journal for Numerical Methods in Fluids, **11** (1990), 1015-1031.

[10] M. J. Crochet, R. Keunings, Die swell of a Maxwell fluid: numerical prediction, Journal of Non-Newtonian Fluid Mechanics, **7** (1980), 199-212.

[11] M. J. Crochet, R. Keunings, Finite element analysis of die swell of a highly elastic fluid, Journal of Non-Newtonian Fluid Mechanics **10** (1982), 339-356.

[12] V. Delvaux, M. J. Crochet, Numerical simulation of delayed die swell, Rheologica Acta, **29** (1990), 1-10.

[13] C. M. Oishi, M. F. Tomé, José A. Cuminato, S. McKee, An implicit technique for solving 3D low Reynolds number moving free surface flows, Journal of Computational Physics, **227** (2008), 7446-7468.

[14] A. Bonito, M. Picasso, M. Laso, Numerical simulation of 3D viscoelastic flows with free surfaces, JCP (215 (2006), 691-716.

[15] M. A. Alves, P. Oliveira, F. Pinho, A convergent and universally bounded interpolation scheme for the treatment of advection, International Journal for Numerical Methods in Fluids, **41** (2003), 47-75.

[16] M. F. Tomé, L. Grossi, , A. Castelo, J. A. Cuminato, S. McKee, K. Walters, Dieswell, splashing drop and a numerical technique for solving the Oldroyd B model for axisymmetric free surface flows, Journal of Non-Newtonian Fluid Mechanics, **141**, (2007), 148-166.

[17] M. F. Tomé, A. Castelo, J. Murakami, J. A. Cuminato, R. Minghin, M. C. F. Oliveira, N. Mangiavacchi, S. McKee, Numerical simulation of Axisymmetric free surface flows, Journal of Computational Physics, **157** (2000), 441-472.

[18] J. Peng, K.-Q. Zhu, Instability of the interface in co-extrusion flow of two UCM fluids in the presence of surfactant, Journal of Non-Newtonian Fluid Mechanics, **166** (2011), 152-163.

[19] R. A. Figueiredo, C. M. Oishi, J. A. Cuminato, J. C. Azevedo, A. M. Afonso, M. A. Alves, Numerical investigation of three dimensional viscoelastic free surface flows: impacting drop problem, Proceedings of 6th European Conference on Computational Fluid Dynamics (ECFD VI), E. Onate, J. Oliver and A. Huerta (Eds), 2014, Barcelona, Spain.

[20] Xi. Xu, J. Ouyang, T. Jiang, Q. Li, Numerical simulation of 3D-unsteady viscoelastic free surface flows by improved smoothed particle hydrodynamics method, Journal of Non-Newtonian Fluid Mechanics, **177-178**, (2012), 109-120.

[21] H. Jasak, A. Jemcov, Z. Tukovic, OpenFOAM: a C++ library for complex physics simulations, International Workshop on Coupled Methods in Numerical Dynamics, IUC Dubrovnik, Croatia, 2007, 1-20.

[22] D. Rajagopalan, R. C. Armstrong, R. A. Brown, Finite Element Methods for calculating of steady, viscoelastic flow using constitutive equations with a newtonian viscosity, J. Non-Newtonian Fluid Mechanics, **36** (1990), 159-192.

[23] Xiaoyang Xu, Xiao-Long Deng, An improved weakly compressible SPH method for simulating free surface flows of viscous and viscoelastic fluids, Computer Physics Communications, **201** (2016), 43-62.

[24] A. J. Chorin, Numerical solution of the Navier-Stokes equations, Mathematics of Computation, **22** (1968), 745-762, DOI: https://doi.org/10.1090/S0025-5718-1968-02423.

[25] M. F. Tomé, B. Duffy, S. McKee, A numerical technique for solving unsteady non-Newtonian free surface flows, Journal of Non-Newtonian Fluid Mechanics, **62** (1996), 9-34.